

# Estimation of Bulk Permittivity of the Moon's Surface Using Lunar Radar Sounder On-board Selenological and Engineering Explorer

**Keigo Hongo**

Division of Earth and Planetary sciences, Graduate School of Science, Kyoto University

**Hiroaki Toh** (✉ [toh@kugi.kyoto-u.ac.jp](mailto:toh@kugi.kyoto-u.ac.jp))

Graduate School of Science, Kyoto University <https://orcid.org/0000-0003-3914-5613>

**Atsushi Kumamoto**

Department of Geophysics, Graduate School of Science, Tohoku University

---

## Full paper

**Keywords:** Selenological and Engineering Explorer, frequency modulated continuous wave radar, bulk permittivity, loss tangent, subsurface reflectors

**Posted Date:** August 7th, 2020

**DOI:** <https://doi.org/10.21203/rs.3.rs-20561/v3>

**License:**  This work is licensed under a Creative Commons Attribution 4.0 International License.

[Read Full License](#)

---

**Version of Record:** A version of this preprint was published on September 22nd, 2020. See the published version at <https://doi.org/10.1186/s40623-020-01259-2>.

1 **Estimation of Bulk Permittivity of the Moon's Surface Using**  
2 **Lunar Radar Sounder On-board Selenological and**  
3 **Engineering Explorer**

4 Keigo Hongo, Division of Earth and Planetary Sciences, Graduate School of Science,  
5 Kyoto University

6 Hiroaki Toh, Division of Earth and Planetary Sciences, Graduate School of Science,  
7 Kyoto University

8 Atsushi Kumamoto, Department of Geophysics, Graduate School of Science, Tohoku  
9 University

10 **Corresponding Author: Hiroaki Toh**

11

## 12 **Abstract**

13           Site-dependent bulk permittivities of the lunar uppermost media with  
14 thicknesses of tens to hundreds meters were estimated based on the data from Lunar  
15 Radar Sounder onboard the Selenological and Engineering Explorer (SELENE). It  
16 succeeded in sounding almost all over the Moon's surface in a frequency range around  
17 5 MHz to detect subsurface reflectors beneath several lunar maria. However, it is  
18 necessary to estimate the permittivity of the surface regolith of the Moon in order to  
19 determine the actual depths to those reflectors instead of apparent depths assuming a  
20 speed of light in the vacuum. In this study, we determined site-dependent bulk  
21 permittivities by two-layer models consisting of a surface regolith layer over a half-  
22 space with uniform but different physical properties from the layer above. Those  
23 models consider the electrical conductivity as well as the permittivity, whose trade-off  
24 was resolved by utilizing the correlation between iron-titanium content and measured  
25 physical properties of lunar rock samples. Distribution of the iron-titanium content on  
26 the Moon's surface had already been derived by spectroscopic observation from  
27 SELENE as well.

28                   Four lunar maria, Mare Serenitatis, Oceanus Procellarum, Mare Imbrium, and  
29 Mare Crisium, were selected as regions of evident reflectors, where we estimated the  
30 following four physical properties of each layer, i.e., bulk permittivity, porosity, loss  
31 tangent and electrical conductivity to conclude the actual depths of the reflectors are  
32 approximately 200m on average. The bulk permittivity ranges from 2.96 at Mare  
33 Imbrium to 6.37 at Oceanus Procellarum, whereas the porosity takes the values between  
34 1.8% to 41.1% in the respective maria. It was found that although the bulk  
35 permittivity of the four lunar maria differs from a mare to a mare, it shows a good  
36 correlation with their composition, viz., their iron-titanium content.

37

## 38 **Keywords**

39 Selenological and Engineering Explorer, frequency modulated continuous wave radar,  
40 bulk permittivity, loss tangent, subsurface reflectors

41

## 42 **1. Introduction**

43                   The first exploration of the Moon's subsurface structure was conducted by

44 Apollo Lunar Sounder Experiment (ALSE) (Porcello et al., 1974) aboard Apollo 17  
45 launched in 1972. ALSE observed the reflected echoes of the radar transmitted from  
46 the mother ship orbiting above the lunar equator. Objectives of ALSE were subsurface  
47 exploration of the Moon and profiling/imaging of its surface. To achieve those, ALSE  
48 was operated at a few frequency bands of 5, 15 and 150MHz with linearly increasing  
49 frequency (chirp signals) so as to improve the penetration depth and the ranging  
50 resolution. The largest penetration depth of approximately 1.3km was achieved by the  
51 5MHz operation with an apparent resolution of 300m. However, both the depth and  
52 the resolution are dependent on the permittivity inside the Moon. ALSE detected  
53 horizontal reflectors at an apparent depth of about 1km beneath Mare Serentatis and  
54 Mare Crisium (Peeples et al., 1978; Phillips et al., 1973a, b) by its limited observation  
55 from several orbits.

56 Lunar Radar Sounder (LRS) is a Frequency Modulated Continuous Wave  
57 radar (Ono and Oya, 2000) equipped with SELenological and ENgineering Explorer  
58 (SELENE) launched in 2007 (Kato et al., 2008). Because it was the first Japanese  
59 spacecraft to the Moon, it also has a Japanese name of KAGUYA coined after a

60 princess believed to live on the Moon. Like ALSE, LRS also aimed at subsurface  
61 exploration of the Moon using high frequency chirp signals ranging from 4 through  
62 6MHz. Major differences, however, from ALSE were its deeper penetration depth and  
63 finer resolution, which were 5km and 75m in vacuum and were much better than those  
64 of ALSE (Ono and Oya, 2000; Ono et al., 2008). Spatial coverage of SELENE was  
65 excellent in the sense that almost all of the Moon's surface including the far side was  
66 covered by the sounder observation from SELENE's polar orbits with an averaged  
67 altitude of 100km above the Moon's surface. The total duration of the sounder  
68 observation summed up to as long as 100 days. As a result, Ono et al. (2009) reported  
69 presence of subsurface reflectors beneath several lunar maria. Apparent depths to  
70 those reflectors were a few hundreds of meters but we need to know the permittivity  
71 beneath the Moon's surface for conversion of those values to the true depths.  
72 Furthermore, quantitative delineation of the Moon's subsurface structure such as the  
73 true depths to the reflectors leads to understanding the origin and evolution of our  
74 Moon. It, therefore, is very important to analyze the LRS data of SELENE, which  
75 provided unprecedented radar sounding in terms of both quality and quantity.

76                   Another example of planetary radar sounding can be found in Mars. Mars  
77   Advanced Radar for Subsurface and Ionosphere Sounding on-board Mars Express in  
78   2003 detected presence and quantity of water ice accumulated in the Mars's polar cap  
79   (Picardi et al., 2005; Plaut et al., 2007). Presence of water ice on Mars was further  
80   confirmed by Shallow Radar Sounder aboard Mars Reconnaissance Orbiter in 2005.  
81   Karlsson et al. (2015) found the water ice even in Mars's mid-latitudes, while Holt et al.  
82   (2010) revealed a complex sedimentary structure beneath the Mars's northern polar cap.  
83   These new findings are expected to elucidate the past Mars's climate and/or traces of  
84   paleo-oceans on Mars.

85                   On the other hand, JUpiter ICy moon Explorer (JUICE) by European Space  
86   Agency (ESA) is planned to launch in 2022. According to ESA (2014), Radar of Icy  
87   Moon Exploration aboard JUICE is going to conduct radar sounding of three icy  
88   Galilean satellites, i.e., Europa, Ganymede and Calisto so as to explore the subsurface  
89   structures, ice, water and their composition. Those sounding will be of great help for  
90   detecting subsurface oceans of those moons, which may constitute cradles for  
91   extraterrestrial lives.

92                    Unlike the sample return missions, the past and future radar sounding from  
93 spacecraft illustrates efficiency, certainty and wide spatial coverage of planetary-scale  
94 exploration by radar sounders. In order to improve applicability of radar sounding, the  
95 LRS data have been combined with model calculation of electromagnetic (EM) wave  
96 propagation (Ono et al., 2009; Bando et al., 2015) and data by laser altimetry to estimate  
97 the thickness of the regolith layer on top of the Moon as well as to improve the ranging  
98 resolution of LRS itself by application of data processing techniques originally  
99 developed for synthetic aperture radars (Kobayashi and Ono, 2007; Kobayashi et al.,  
100 2012).

101                    Ono et al. (2009) argued the possibility of detection of the subsurface regolith  
102 layer sandwiched between basaltic layers above and below as reflectors. This is  
103 because the reflectors are detected at shallower depths than the thickness of the basaltic  
104 layers estimated by crater analyses in lunar maria (De Hon, 1979; Williams and Zuber,  
105 1998). Oshigami et al. (2009) further claimed that the correlation between the surface  
106 age and detection rate of the reflectors means thicker regolith layers in older regions.

107                    Another correlation, which is negative though, between the detection rate and

108 surface distribution of ilmenite suggests that metals such as titanium may prevent  
109 penetration of radar pulses to interfere the reflector detection (Pommerol et al., 2010;  
110 Olhoeft and Strangway, 1975; Carrier et al., 1991; Shkuratov and Bondarenko, 2001).  
111 The composition of the Moon's surface was revealed by spectroscopic studies of  
112 SELENE data. This means that both permittivity and loss tangent are important  
113 physical properties of the lunar surface, because the former determines the speed of  
114 light in the medium while the latter is defined as the ratio of the conduction current to  
115 the displacement current and plays a role in attenuation of the radar pulses. Analyses  
116 of lunar rock samples strongly imply the correlation between the loss tangent and the  
117 iron-titanium content, whereas the permittivity does not show significant dependence on  
118 rock composition. It has, in turn, a strong correlation with rock density (Olhoeft and  
119 Strangway, 1975; Carrier et al., 1991; Shkuratov and Bondarenko, 2001). The  
120 different dependence of physical properties of the Moon's surface suggests regional  
121 dependence of those properties, and thus implies necessity of determination of those  
122 properties from place to place.

123 Porosity is another factor of consideration here. Effects of bulk porosity are

124 inevitably included in the results of radar sounding in a form of bulk density. If we  
125 can also estimate porosity from our LRS data, it can be another important database,  
126 since Rust et al. (1999) pointed out that porosity is indicative of volcanism/tectonics of  
127 the Moon in the past.

128           Ishiyama et al. (2013) performed combined analyses of the delay of echoes  
129 from the subsurface reflectors and the depth of subsurface reflectors excavated at the  
130 impact craters based on data from LRS, Multiband Imager (MI) and Terrain Camera  
131 (TC) onboard the SELENE spacecraft, and determined the speed of the radar wave in  
132 uppermost layers in several maria. Based on the speed, they also estimated bulk  
133 permittivity and porosity. The estimated bulk permittivities were between 1.6 and 14.0  
134 in Mare Serenitatis, and between 1.3 and 5.1 in Oceanus Procellarum. They also pointed  
135 out that the estimated porosity, up to about 80 %, was much larger than that of Apollo  
136 soil samples, and discussed possible contributions of intrinsic voids of lava and impact-  
137 induced cracks.

138           In this study, we aim for estimation of the relative permittivity of the Moon's  
139 surface by comparison of echo intensities from the surface and subsurface reflector.

140 We will approximate the Moon by two-layer models with different permittivities and  
141 electrical conductivities in each layer and determine those model parameters by  
142 calculation of EM wave propagation according to the radar range equation. In the  
143 course of estimation, we newly introduce correlation between the electrical conductivity  
144 and the iron-titanium content to resolve the non-uniqueness appeared in previous  
145 studies. This study will also provide spatial dependence of the true depths to the  
146 detected reflectors, which may lead to better understanding of the Moon's subsurface  
147 structures. Furthermore, those true depths can be applied to estimation of erupted lava  
148 volumes, which are useful in unraveling the Moon's volcanism in the past. Finally,  
149 the estimated loss tangent and porosity contribute to the understandings of the Moon's  
150 evolution and thermal history as well.

151

## 152 **2. Data of Lunar Radar Sounder**

153 A pair of mutually orthogonal 30m dipole antennas was used for LRS. The  
154 pulse width ( $T$ ), sweep rate ( $\dot{f}$ ) and output power ( $P_t$ ) of the transmitted chirp signals  
155 were  $200\mu\text{s}$ ,  $10\text{kHz}/\mu\text{s}$  and  $800\text{W}$ , respectively. Each pulse was further shaped by a

156 sinusoidal wave to minimize sidelobe effects at the time of Fast Fourier Transform

157 (FFT) and is given by:

$$158 \quad V_{TX}(t) = V_{TX0} \sin\left(\pi \frac{t}{T}\right) \sin\left(\int_0^t 2\pi(f_0 + \dot{f}t') dt'\right), \quad (1)$$

159 where  $V_{TX0}$  is the amplitude of the transmitted pulse and  $f_0 = 4\text{MHz}$ .

160 In general, radars are associated with a trade-off between the penetration

161 depth, which is a function of the output power, and the ranging resolution, which is a

162 function of the pulse width. However, the pulse compression technique using chirp

163 signals gives us a radar with a large output power and a narrow pulse width at the same

164 time, which improves both the penetration depth and the ranging resolution. In the

165 case of LRS, they are 5km and 75m in vacuum as mentioned before, but they are also

166 dependent on both the permittivity and the loss tangent beneath the Moon's surface.

167 The LRS operation throughout the mission was done by 20Hz transmission for 72 days,

168 while it was operated with a transmission rate of 2.5Hz for the remaining 27 days. The

169 LRS data are now open to the public at:

170 <http://darts.isas.jaxa.jp/planet/pdap/selene/>,

171 and all the data used in this study were downloaded from this Japan Aerospace

172 Exploration Agency website.

173

## 174 **2.1 A-scope Data**

175 Received echoes of LRS are not original waveforms of the reflected echoes  
176 themselves but resampled waveforms multiplied by a local signal, which were further  
177 transferred to the Earth from the spacecraft. The observed data, therefore, are different  
178 from the original waveforms of the reflected echoes.

179 Specifically, let the original waveform be:

$$180 \quad V_{RX}(t) = V_{RX0} \sin\left(\pi \frac{t - \tau_{RX}}{T}\right) \sin\left(\int_0^{t - \tau_{RX}} 2\pi(f_0 + \dot{f}t') dt'\right), \quad (2)$$

181 where  $V_{RX0}$  is the amplitude of the reflected echo and  $\tau_{RX}$  is a two-way travel time of  
182 the echo, by which the apparent depth to the reflector,  $d_A$ , can be given by:

$$183 \quad d_A = \frac{c_0 \tau_{RX}}{2}, \quad (3)$$

184 where  $c_0$  is the speed of light in vacuum. In chirp radars, the received echoes are  
185 further mixed with an inherent local signal of the receiver typically given by the  
186 following formula:

$$187 \quad V_{LO}(t) = V_{LO0} \sin\left(\int_0^{t - \tau_{LO}} 2\pi(f_0 + \dot{f}t') dt'\right), \quad (4)$$

188 where  $V_{LO0}$  is the amplitude of the local signal and  $\tau_{LO}$  is the time of the mixing onset.

189 The waveform after mixing becomes:

$$\begin{aligned} 190 \quad V_{RX}(t)V_{LO}(t) &= V_{RX0}V_{LO0}\sin\left(\pi\frac{t-\tau_{RX}}{T}\right)\sin\left(\int_0^{t-\tau_{RX}}2\pi(f_0 + \right. \\ 191 \quad \left. \dot{f}t')dt'\right)\sin\left(\int_0^{t-\tau_{LO}}2\pi(f_0 + \dot{f}t')dt'\right) &= V_{RX0}V_{LO0}\sin\left(\pi\frac{t-\tau_{RX}}{T}\right)\sin\left[2\pi\left\{f_0(t-\tau_{RX}) + \right. \right. \\ 192 \quad \left. \left. \frac{1}{2}\dot{f}(t-\tau_{RX})^2\right\}\right]\sin\left[2\pi\left\{f_0(t-\tau_{LO}) + \frac{1}{2}\dot{f}(t-\tau_{LO})^2\right\}\right]. \quad (5) \end{aligned}$$

193 Using a formula for the trigonometric functions, Eq. (5) can be further modified into a  
194 sum of the high frequency part and the low frequency part as:

$$\begin{aligned} 195 \quad V_{RX}(t)V_{LO}(t) &= -\frac{1}{2}V_{RX0}V_{LO0}\sin\left(\pi\frac{t-\tau_{RX}}{T}\right)\left(\cos\left[2\pi\left\{f_0(2t-\tau_{RX}-\tau_{LO}) + \right. \right. \right. \\ 196 \quad \left. \left. \frac{1}{2}\dot{f}(2t^2+\tau_{RX}^2-2(\tau_{RX}+\tau_{LO})t+\tau_{LO}^2)\right\}\right] - \cos\left[2\pi\left\{\dot{f}(\tau_{RX}-\tau_{LO})t + \right. \right. \\ 197 \quad \left. \left. f_0(\tau_{RX}-\tau_{LO}) - \frac{1}{2}\dot{f}(\tau_{RX}^2-\tau_{LO}^2)\right\}\right]). \quad (6) \end{aligned}$$

198 Equation (6) is then low-pass filtered with a cut-off frequency of 2MHz to eliminate the  
199 first term in the right hand side (R.H.S.) and resampled for 2048 points with a sampling  
200 frequency of 6.25MHz. Figure 1 shows a sample plot of thus processed and  
201 transferred to the Earth.

202 Although filtered and resampled, the waveforms of the reflected echoes  
203 preserve the information of the two-way travel times in the form of frequency.

204 Namely, if one makes Fourier transforms of the echoes and finds specific frequencies,

205  $f_{IF}$ 's, for each peak reflection, then the following relation holds:

206 
$$f_{IF} = \dot{f}(\tau_{RX} - \tau_{LO}). \quad (7)$$

207 Equations (3) and (7) are combined to give:

208 
$$d_A = \frac{c_0 \tau_{RX}}{2} = \frac{c_0 \tau_{LO}}{2} + \frac{c_0 f_{IF}}{2\dot{f}}. \quad (8)$$

209 The first term on R.H.S. of Eq. (8) is called the 'altitude origin for ranging' and

210 recorded in the LRS data together with the received waveform itself, the time stamp, the

211 selenographic latitude/longitude and the spacecraft's altitude. Figure 2(a) shows

212 Fourier transforms of the reflected echo shown in Fig.1. Plots of this kind are called

213 'A-scope'. In Fig. 2(b), three echoes are evident, one is from the Moon's surface and

214 the other two from the subsurface reflectors.

215

## 216 **2.2 B-scan Data**

217 B-scan is a sort of dynamic spectrum using A-scope with echo intensity in

218 color, and is called 'radargram', a pseudo section of the Moon's subsurface structure.

219 Figure 3(a) shows a B-scan image over Mare Imbrium. The height of the steps seen on

220 the Moon's surface is approximately 75m, which is in good harmony with the ranging  
221 resolution of LRS in vacuum.

222           Reflected echoes do not always come from the nadir direction. If there is  
223 significant undulation of the Moon's surface, the subsurface reflectors are possibly  
224 masked by strong reflected echoes on the surface. Figure 3(b) shows a typical  
225 example of the surface echoes, which have clear parabolic shapes because the distance  
226 between the spacecraft and the reflection points on the Moon's surface can vary with  
227 time as the spacecraft maneuvers along its orbit.

228           Taking running means on the B-scan images is known to give a better  
229 protection against the surface echoes (Ono et al., 2010), provided that the subsurface  
230 reflectors are horizontal. It is also desirable to compare the running means of adjacent  
231 orbits so as to confirm the echoes coming from not 'surface' but 'subsurface'. Figure  
232 3(c) shows a B-scan image by taking a running mean of successive 21 raw B-scan  
233 images (Ono et al., 2010). It is noteworthy that the continuity of the subsurface  
234 reflectors is much clearer than Fig. 3(a).

235

## 236 3. Methods

### 237 3.1 Two-layer Model

238 Because the regions with two subsurface reflectors like the one shown in Fig.  
239 3(c) were very limited, we decided to model the majority of the LRS data by two layers,  
240 which the transmitted waves entered normal to the surface. Figure 4 shows a  
241 schematic diagram of the assumed model. Using the radar range equation (e.g.,  
242 Phillips, 1973a), the reflected powers,  $P_{rs}$  and  $P_{rSS}$ , are respectively given by:

$$243 \quad P_{rs}(\varepsilon_1) = \frac{P_t G^2 \lambda^2}{4(4\pi R)^2} r_{01}, \quad (9)$$

244 and

$$245 \quad P_{rSS}(\varepsilon_1, \varepsilon_2, \sigma_1) = \frac{P_t G^2 \lambda^2}{4[4\pi(R+R_D)]^2} e^{-2\omega \frac{R_D}{c_1} \tan \delta_1} t_{01} r_{12} t_{10}, \quad (10)$$

246 where  $G$ ,  $\lambda$ ,  $\omega$ ,  $\tan \delta_1$ , and  $R_D$  are the gain of the antenna, the wavelength and angular  
247 frequency of the transmitted wave, the loss tangent of the first layer and the true  
248 thickness of the first layer, respectively. **SELENE transmitted a radar pulse every 0.05**  
249 **(or 0.4) second with an output power of  $P_t$  [W].**  $c_1$  is the speed of light in the first  
250 layer and given by:

$$251 \quad c_1 = \frac{1}{\sqrt{\varepsilon_1 \varepsilon_0 \mu_0}} = \frac{c_0}{\sqrt{\varepsilon_1}} \quad (11)$$

252 where  $\varepsilon_0$  and  $\mu_0$  are the permittivity and magnetic permeability in vacuum, respectively.

253 The loss tangent in the first layer can be written by:

254 
$$\tan\delta_1 = \frac{\sigma_1}{\omega\varepsilon_0\varepsilon_1}, \quad (12)$$

255 as well.  $r_{ij}$  and  $t_{ij}$  ( $i, j = 0, 1, 2$ ) denote the reflection and transmission coefficients at

256 each interface and satisfy the following relation according to the Fresnel equations:

257 
$$t_{01} = t_{10} = \frac{4\sqrt{\varepsilon_1}}{(1+\sqrt{\varepsilon_1})^2}, \quad (13)$$

258 
$$r_{01} = \left(\frac{1-\sqrt{\varepsilon_1}}{1+\sqrt{\varepsilon_1}}\right)^2, \quad (14)$$

259 
$$r_{12} = \left(\frac{\sqrt{\varepsilon_1}-\sqrt{\varepsilon_2}}{\sqrt{\varepsilon_1}+\sqrt{\varepsilon_2}}\right)^2. \quad (15)$$

260 Equation (15) allows solutions of both  $\varepsilon_1 > \varepsilon_2$  and  $\varepsilon_1 < \varepsilon_2$ . However, if one

261 takes  $\varepsilon_1 > \varepsilon_2$ , it yields  $1 < \varepsilon_2 < 2$ , which is incompatible with the results of the

262 Moon rock analyses (e.g., Olhoeft and Strangway, 1975). It, therefore, is assumed

263  $\varepsilon_1 < \varepsilon_2$  throughout this study. **As for other parameters such as  $R$  [m], refer to Fig. 4**

264 **and its caption.**

265

### 266 **3.2 Correlation among Physical Properties**

267 The previous analyses of the lunar rock samples (Shkuratov and Bondarenko,

268 2001; Olhoeft and Strangway, 1975) revealed correlation among the physical properties  
269 of the rocks such as loss tangent, density, permittivity and iron-titanium content. In  
270 short, they are expressed by the following formulae:

$$271 \quad \tan\delta = 8.8 \times 10^{-4} e^{\frac{1-p}{2}\rho_{grain}(S)+0.085S}, \quad (16)$$

$$272 \quad \rho_{grain}(S) = 0.0165S + 2.616, \quad (17)$$

$$273 \quad \varepsilon = 1.919\rho, \quad (18)$$

274 where  $S$ ,  $p$  and  $\rho$  are the total content of titanium and iron [wt%], porosity and density  
275 [ $10^{-3}$  kg  $m^{-3}$ ], respectively. The subscript, grain, denotes the properties of the material  
276 itself. The porosity is defined by:

$$277 \quad \rho = \rho_{grain}(1 - p). \quad (19)$$

278 The bulk estimate of permittivity in the 1<sup>st</sup> layer,  $\varepsilon_1$ , should also be compared with  $\varepsilon_{grain}$ .

279

### 280 **3.3 Flow of Data Analysis**

281 First, the following quantities are considered as constants:  $P_t = 800W$ ,  $\lambda =$   
282  $0.06km$  for the center frequency (5MHz) for a range of 4-6MHz and  $G = 1.64$  from the  
283 theoretical value of the dipole antenna. It follows from Eqs. (9), (14) and observed  $P_{rs}$

284 that  $\varepsilon_1$  can be determined. Equation (18) allows us to convert thus obtained  $\varepsilon_1$  to  $\rho$ .

285 Lawrence et al. (2002) analyzed the spectroscopic data by Lunar Prospector to  
286 yield 5° by 5° grid data of the surface content of iron and titanium as:

287 [http://pds-geosciences.wustl.edu/lunar/lp-1-grs-5-elem-abundance-  
v1/lp\\_9001/data/lpgrs\\_high1\\_elem\\_abundance\\_5deg.tab](http://pds-geosciences.wustl.edu/lunar/lp-1-grs-5-elem-abundance-<br/>288 v1/lp_9001/data/lpgrs_high1_elem_abundance_5deg.tab)

289 Substitution of the above iron and titanium contents ( $S$ ) into Eq. (17) gives  $\rho_{\text{grain}}$ .

290 Once  $\rho$  and  $\rho_{\text{grain}}$  are known, the porosity,  $p$ , can be estimated using Eq. (19). The

291 remaining model parameters,  $\sigma_1$  and  $\varepsilon_2$ , can be determined using Eqs. (10), (12) and

292 (16) in addition to observed  $P_{\text{rss}}$  as shown in the flow chart (Fig. 5).

293 In this analysis, we need absolute values of the echo powers in unit of W.

294 They are determined based on the prelaunch calibration of the LRS's receiver. Of

295 course, it was not confirmed by the end-to-end calibration including extended antenna

296 and spacecraft because such test was quite difficult to perform on the ground. So, we

297 roughly check validity of the absolute calibration of the echo powers used in this study

298 by comparison between bulk permittivities estimated in Ishiyama et al. (2013) and those

299 in this study (see Section 5.1).

300

## 301 **4. Results**

### 302 **4.1 Analyzed Regions**

303           We analyzed four lunar maria, viz., Mare Serenitatis, Oceanus Procellarum,  
304 Mare Imbrium, and Mare Crisium. This is partly because clear subsurface reflectors  
305 were recognized by radargrams of several adjacent orbits in those lunar maria, and  
306 partly because it is difficult to completely eliminate the effect of surface echoes, which  
307 are especially intense in the highland areas of the Moon. Figure 6 shows the four  
308 target regions **under** study. Note that the values described in this section are mainly field  
309 **estimates of bulk properties.**

310

### 311 **4.2 Estimated Physical Properties of All Maria**

312           Because reflected echoes from the Moon's surface were observed  
313 everywhere, the bulk permittivity of the first layer,  $\epsilon_1$ , was estimated using Eq. (9) **for**  
314 371 shots, which were approximately equivalent to one selenographic latitude.  $\epsilon_{\text{grain}}$   
315 was estimated using Eqs. (17) and **(18) together with** the iron-titanium content of this

316 region by Lawrence et al. (2002).

317 Unlike the surface echoes, the subsurface echoes were not always detected.

318 To circumvent this, 21 stacks of A-scope were taken using the surface echo as a

319 reference. Figure 7 shows an example of the stacked A-scope. Using those stacked

320 echoes, estimates of  $\varepsilon_2$  were obtained in the respective latitudinal ranges using the

321 previously estimated  $\varepsilon_1$  and Eq. (10).

322 Radargrams of all regions are shown in Figs. 8, 10, 12 and 14, while estimates

323 of  $\varepsilon_1$ ,  $\varepsilon_2$ , and  $\varepsilon_{\text{grain}}$  are plotted in Figs. 9, 11, 13 and 15 for lunar maria **under study**.

324 Table 1 shows estimated porosity (%), loss tangent, electrical conductivity (S/m) in

325 addition to the derived relative permittivities. The Fe + Ti content,  $S$  (wt%), tabulated in

326 Table1 was used to estimate  $\varepsilon_{\text{grain}}$ . The table also includes the averaged apparent depths

327 (m) as well as the calculated actual depths (m), and the number of identified subsurface

328 echoes. In Mare Serenitatis and Oceanus Procellarum, the derived ranges of  $\varepsilon_1$  are

329 almost compatible with those reported by Ishiyama et al. (2013): **1.6 ~ 14.0 and 1.3 ~**

330 **5.1**.

331

### 332 **4.3 Summary of Data Analyses**

333 All results described in this section are summarized in Table 1 along with  
334 estimated ages of the lunar maria determined by crater density (Hiesinger et al., 2000;  
335 2003; 2011). Values of the bulk permittivity show correlation with  $S$ . Table 1 also  
336 shows that each tabulated value has small spatial variation in the latitude difference of  
337  $5^\circ$  to  $10^\circ$ . Figure 16 was created from Table 1 using values of  $\varepsilon_1$  and their 95 %  
338 confidence intervals shown in Figs. 9, 11, 13, and 15. Table 1 shows a clear positive  
339 correlation of the bulk permittivity,  $\varepsilon_1$ , derived in this study with the reported Fe and Ti  
340 content,  $S$  (Lawrence et al., 2002). The bulk permittivity can be expressed by  $\varepsilon_1 =$   
341  $0.297 S + 0.0107$  with a correlation coefficient of  $R^2 = 0.881$ .

342

## 343 **5. Discussion**

### 344 **5.1 Validity of Applied Methods**

345 Because many of A-scope data showed peaks of a single subsurface reflector  
346 that can be identified on adjacent orbits as well, it is reasonable to assume two-layer  
347 models for the LRS data. However, the analyzed results show that there are several

348 regions of anomalously large errors for bulk permittivity. It is very difficult to  
349 consider those errors due to actual spatial variations of  $\epsilon_1$  and  $\epsilon_2$ . It can be rather  
350 interpreted as a result of scattering of surface echoes by rugged topography. The  
351 radargrams over the large error regions suggest that those regions are characterized by  
352 combinations of intense and weak echoes. In this study, relatively flat regions were  
353 selected to yield radargrams by taking running means for better protection against  
354 rugged topography. However, the results showed that it is not sufficient for all  
355 regions. It, therefore, will be desirable to do more accurate numerical simulations of  
356 EM wave propagation by incorporating known topography on the Moon's surface, to  
357 estimate more precise bulk permittivity over broader regions in the future. As confirmed  
358 in Subsections 4.2 and 4.3, the bulk permittivities derived in Mare Serenitatis and  
359 Oceanus Procellarum in this study were almost in the range reported in Ishiyama et al.  
360 (2013).

361

## 362 **5.2 Bulk Permittivity**

363 The derived bulk permittivity of the lunar uppermost layer was in a range

364 from 2.96 (at Mare Imbrium) to 6.37 (at Oceanus Procellarum), which supports the  
365 actual depth to the reflectors in those maria to be around 200 m.

366           Olhoeft and Strangway (1975), and Carrier et al. (1991) reported that the bulk  
367 permittivity of the Moon rock samples shows values ranging from 1.1 to 11, majority of  
368 which falls between 4 and 9. However, this study yields somewhat smaller bulk  
369 permittivity not only in Mare Serenitatis and Oceanus Procellarum, which was already  
370 reported by Ishiyama et al. (2013), but also in Mare Imbrium and Mare Crisium. This  
371 can be partly attributed to the effect of porosity as discussed by Ishiyama et al. (2013)  
372 but also explained by the effect of composition, i.e., iron-titanium content.

373           Olhoeft and Strangway (1975) showed that the bulk permittivity is primarily a  
374 strong function of bulk density. This means that the bulk permittivity depends on not  
375 only how porous the medium in concern is, but also how dense and dielectric the rest of  
376 the medium other than cavity is. Titanium bearing minerals such as ilmenite is typical  
377 of those that have both large density and high permittivity. The good correlation  
378 between the bulk permittivity derived in this study and the known FeO + TiO<sub>2</sub> content  
379 of the lunar maria surface shown in Fig. 16 can be regarded as possible presence of

380 enriched titanium bearing minerals in each lunar mare such as Mare Imbrium.

381           The analysis method used in this study enabled us to derive bulk permittivity

382 and porosity in wide area of multiple maria. A new suggestion brought by the

383 comparison of porosity in multiple maria in this study will be described in the next

384 subsection. The estimates of  $\varepsilon_2$  showed larger shot-by-shot scatter than  $\varepsilon_1$ . It was

385 assumed throughout this study that  $\varepsilon_1 < \varepsilon_2$  in applying the two-layer models.

386 However, its validity for multiple layer models should be examined in the future.

387

### 388 **5.3 Porosity**

389           Based on the bulk permittivity from 2.96 to 6.37, the porosity takes the values

390 between 1.8% to 41.1%. Porosity of the Moon rock samples is less than 10% in most

391 cases, and hence samples with porosity larger than 20% are rare (Olhoeft and

392 Strangway, 1975). However, this study yielded larger porosity, which possibly

393 represents macroscopic (bulk) porosity rather than microscopic as was pointed out by

394 Ishiyama et al. (2013).

395           Sizes of the Moon rock samples are of the order of centimeter, while the

396 spatial resolution of LRS is at most a few tens of meters. This means that the LRS  
397 data are subject to effects of large-scale cracks. Hence, the large bulk porosity may be  
398 due to cracks by degassing at the time of volcanic eruptions, by quenching of lavas or  
399 by meteorite impacts. However, it turned out that porosity shows a weak negative  
400 correlation with formation ages of lunar maria (see Fig. 17). This may reflect effects of  
401 volcanic eruptions rather than those of meteorite impacts, because repeated meteorite  
402 impacts might have cultivated the Moon's surface well enough to give a 'positive'  
403 correlation with formation age.

404

#### 405 **5.4 Loss Tangent**

406 The estimated range of loss tangent was  $5.3 \times 10^{-3}$  -  $1.53 \times 10^{-2}$  in this study.  
407 Olhoeft and Strangway (1975) derived a range of  $7.53 \times 10^{-3}$  -  $1.92 \times 10^{-2}$  at (Fe + Ti  
408 wt%) = 15 by their laboratory experiments of the Moon rock samples. The smaller  
409 loss tangent range of this study may also be attributed to the macroscopic porosity.  
410 Substitution of (Fe + Ti wt%) = 15 into Eqs. (16) and (17) yields a width of  $4.6 \times 10^{-3}$   
411 for the loss tangent range, if porosity is changed from 0% through 30%. If the

412 observed loss tangent is corrected by this range width, the two ranges, i.e., the field and  
413 laboratory ranges, agree very well. Furthermore, Bando et al. (2015) investigated the  
414 ratio between the powers of echoes from subsurface reflectors at different depths  
415 measured by LRS to yield a loss tangent range of  $1.07 \times 10^{-2}$  -  $1.13 \times 10^{-2}$ , which  
416 corresponds to the median value of the observed loss tangent by this study. It,  
417 therefore, can be concluded that the loss tangent by this study may reflect the true loss  
418 tangent near the lunar surface (10 ~ 100m spatial scale) with possible variations  
419 produced by macroscopic porosity.

420

## 421 **6. Conclusions**

422 Assuming incident EM waves from LRS being normal to the horizontally  
423 stratified two-layer models, bulk permittivity, porosity and loss tangent near the lunar  
424 surface were estimated using the observed LRS data by calculating EM wave  
425 propagation according to the radar range equation. Combined use of the estimated  
426 FeO + TiO<sub>2</sub> content distribution by spectroscopy of the lunar surface (Lawrence et al.,  
427 2002) and the empirical relations among physical quantities in concern derived from

428 analyses of the Moon rock samples (Shkuratov and Bondarenko, 2001; Olhoeft and  
429 Strangway, 1975) enabled unique determination of otherwise degenerated physical  
430 quantities. The results are summarized in Table 1, in which all the analyzed regions,  
431 viz., Mare Imbrium, Oceanus Procellarum, Mare Crisium and Mare Serenitatis, are  
432 included. It is obvious by the table that the actual depth to the subsurface reflectors of  
433 the Moon is around 200m except for Mare Crisium and one part of Mare Serenitatis.

434           The estimates of each physical quantity do not change much within a  
435 latitudinal difference of 5° to 10°, whereas bulk permittivity shows a positive correlation  
436 with FeO + TiO<sub>2</sub> content. Since porosity, in turn, shows a weak negative correlation  
437 with formation ages of lunar maria (see Fig. 17), it may reflect effects of volcanic  
438 eruptions rather than those of meteorite impacts. Finally, Table 1 will make a good  
439 reference for future studies, because discrepancy between the field and laboratory  
440 estimates is turned out to be reconciled by the effect of porosity.

441

## 442 **Declarations**

443           **List of abbreviations**

444 ALSE: Apollo Lunar Sounder Experiment

445 EM: electromagnetic

446 ESA: European Space Agency

447 JUICE: JUpter ICy moon Explorer

448 LRS: Lunar Radar Sounder

449 RIME: Radar of Icy Moon Exploration

450 SELENE: SELEnological and ENgineering Explorer

451 **Availability of data and materials**

452 The datasets used and/or analyzed during the current study are available

453 from the following links:

454 The LRS data:

455 <http://l2db.selene.darts.isas.jaxa.jp/>

456 The Fe and Ti content distribution:

457 [http://www.mapaplanet.org/data\\_local/Lunar\\_Pro prospector/lp\\_fe\\_5d.asc](http://www.mapaplanet.org/data_local/Lunar_Pro prospector/lp_fe_5d.asc)

458 [http://www.mapaplanet.org/data\\_local/Lunar\\_Pro prospector/lp\\_ti\\_5d.asc](http://www.mapaplanet.org/data_local/Lunar_Pro prospector/lp_ti_5d.asc)

459 **Competing interests**

460 The authors declare that they have no competing interests.

461 **Funding**

462 This work was partly supported by JSPS KAKENHI Grant Number

463 JP25420402.

464 **Authors' contributions**

465 KH carried out data processing, modelling and figure and table drawings.

466 HT supervised KH throughout this study to achieve a master degree, and

467 converted his master thesis in Japanese to the draft manuscript in

468 English. AK guided the data processing and modelling by providing

469 raw time-series of reflected echoes together with their metadata and

470 necessary information for modelling/interpretation. All authors read

471 and approved the final manuscript.

472 **Acknowledgements**

473 We are indebted to Professors A. Yamaji at Graduate School of Science,

474 Kyoto University and M. Yamamoto at Research Institute for Sustainable

475 Humanosphere, Kyoto University for their help that was indispensable to

476 complete this work.

477 **Authors' information**

478 Keigo Hongo, Division of Earth and Planetary Sciences, Graduate School

479 of Science, Kyoto University

480 Hiroaki Toh, Division of Earth and Planetary Sciences, Graduate School

481 of Science, Kyoto University

482 Atsushi Kumamoto, Department of Geophysics, Graduate School of

483 Science, Tohoku University

484 Corresponding Author: Hiroaki Toh

485

486 **References**

487 Bando Y., Kumamoto A., and Nakamura N. Constraint on subsurface structures beneath

488 Reiner Gamma on the moon using the KAGUYA lunar radar sounder. *Icarus*, 254:144-

489 149, 2015.

490 Carrier W. D., Olhoeft, G. R., and Mendell, W. Physical properties of the lunar surface.

491 Lunar Sourcebook, pp. 475-594, 1991.

492 De Hon, R. A. Thickness of the western mare basalts. In Lunar and Planetary Science  
493 Conference Proceedings, Vol. 10, pp. 2935-2955, 1979.

494 ESA/SRE, JUICE definition study report (red book). 2014.

495 Hiesinger, H., Head, J., Wolf, U., Jaumann, R., and Neukum, G. Ages and stratigraphy  
496 of mare basalts in Oceanus Procellarum, Mare Nubium, Mare Cognitum, and Mare  
497 Insularum. *J. Geophys. Res.*, 108(E7), 5065, doi:10.1029/2002JE001985, 2003.

498 Hiesinger, H., Jaumann, R., Neukum, G., and Head, J. W. Ages of mare basalts on the  
499 lunar nearside. *J. Geophys. Res.*, 105(E12):29239-29275, 2000.

500 Hiesinger, H., Bogert, C. van der, Reiss, D., and Robinson, M. Absolute model ages of  
501 basalts in Mare Crisium. In EPSC-DPS Joint Meeting 2011, Vol. 1, p. 1095, 2011.

502 Holt, J., Fishbaugh, K., Byrne, S., Christian, S., Tanaka, K., Russell, P., Herkenhoff, K.,  
503 Safaeinili, A., Putzig, N., and Phillips, R. The construction of Chasma Boreale on Mars.  
504 *Nature*, 465(7297):446-449, 2010.

505 Ishiyama K., Kumamoto, A., Ono, T., Yamaguchi, Y., Haruyama, J., Ohtake, M.,  
506 Katoh, Y., Terada, N., and Oshigami, S. Estimation of the permittivity and porosity of  
507 the lunar uppermost basalt layer based on observations of impact craters by SELENE. *J.*

508 Geophys. Res., 118(7):1453-1467, 2013.

509 Karlsson, N., Schmidt, L., and Hvidberg, C. Volume of Martian midlatitude glaciers  
510 from radar observations and ice flow modeling. Geophys. Res. Lett., 42(8):2627-2633,  
511 2015.

512 Kato, M., S. Sasaki, K. Tanaka, Y. Iijima, Y. Takizawa, The Japanese lunar mission  
513 SELENE: Science goals and present status, Advances in Space Research, 42(2), 294-  
514 300, 2008. <https://doi.org/10.1016/j.asr.2007.03.049>.

515 Kobayashi, T., Kim, J. H., Lee, S. R., Araki, H., and Ono, T. Simultaneous observation  
516 of lunar radar sounder and laser altimeter of KAGUYA for lunar regolith layer  
517 thickness estimate. Geosci. Remote Sens. Lett., IEEE, 7(3):435-439, 2010.

518 Kobayashi, T., Kim, J.-H., Lee, S. R., Kumamoto, A., Nakagawa, H., Oshigami, S.,  
519 Oya, H., Yamaguchi, Y., Yamaji, A., and Ono, T. Synthetic aperture radar processing of  
520 KAGUYA lunar radar sounder data for lunar subsurface imaging. IEEE Trans. Geosci.  
521 Remote Sens., 50(6):2161-2174, 2012.

522 Kobayashi, T. and Ono, T. Sar/insar observation by an HF sounder. J. Geophys. Res.,  
523 112(E3), 2007.

524 Lawrence, J. D., Feldman, W. C., Elphic, R. C., Little, R., Prettyman, T., Maurice, S.,  
525 Lucey, P. G., Binder, A. B. Iron abundances on the lunar surface as measured by the  
526 Lunar Prospector gamma-ray and neutron spectrometers. *J. Geophys. Res.* 107.  
527 10.1029/2001JE001530, 2002.

528 Olhoeft, G. R. and Strangway, D. Dielectric properties of the first 100 meters of the  
529 moon. *Earth Planet. Sci. Lett.*, 24:394-404, 1975.

530 Ono, T., Kumamoto, A., Kasahara, Y., Yamaguchi, Y., Yamaji, A., Kobayashi, T.,  
531 Oshigami, S., Nakagawa, H., Goto, Y., Hashimoto, K., et al. The lunar radar sounder  
532 (LRS) onboard the KAGUYA (SELENE) spacecraft. *Space Sci. Rev.*, 154(1-4):145-  
533 192, 2010.

534 Ono, T., Kumamoto, A., Nakagawa, H., Yamaguchi, Y., Oshigami, S., Yamaji, A.,  
535 Kobayashi, T., Kasahara, Y., and Oya, H. Lunar radar sounder observations of  
536 subsurface layers under the nearside maria of the moon. *Science*, 323(5916):909-912,  
537 2009.

538 Ono, T., Kumamoto, A., Yamaguchi, Y., Yamaji, A., Kobayashi, T., Kasahara, Y., and  
539 Oya, H. Instrumentation and observation target of the lunar radar sounder (LRS)

540 experiment on-board the SELENE spacecraft. *Earth Planets Space*, 60(4):321-332,  
541 2008.

542 Ono, T. and Oya, H. Lunar radar sounder (LRS) experiment on-board the SELENE  
543 spacecraft. *Earth Planets Space*, 52(9):629-637, 2000.

544 Oshigami, S., Yamaguchi, Y., Yamaji, A., Ono, T., Kumamoto, A., Kobayashi, T., and  
545 Nakagawa, H. Distribution of the subsurface reflectors of the western nearside maria  
546 observed from KAGUYA with lunar radar sounder. *Geophys. Res. Lett.*, 36(18), 2009.

547 Peeples, W. J., Sill, W. R., May, T. W., Ward, S. H., Phillips, R. J., Jordan, R. L.,  
548 Abbott, E. A., and Killpack, T. J. Orbital radar evidence for lunar subsurface layering in  
549 Maria Serenitatis and Crisium. *J. Geophys. Res.*, 83(B7):3459-3468, 1978.

550 Phillips, R., Adams, G., Brown, Jr W., Eggleton, R., Jackson, P., Jordan, R., Linlor, W.,  
551 Peeples, W., Porcello, L., Ryu, J., et al. Apollo lunar sounder experiment. In: *Apollo 17*  
552 preliminary science report (NASA SP-330), pp. 1-26, 1973a.

553 Phillips, R., Adams, G., Brown, Jr W., Eggleton, R., Jackson, P., Jordan, R., Peeples,  
554 W., Porcello, L., Ryu, J., Schaber, G., et al. The apollo 17 lunar sounder. In: *Lunar and*  
555 *Planetary Science Conference Proceedings*, Vol. 4, p. 2821, 1973b.

556 Picardi, G., Plaut, J. J., Biccari, D., Bombaci, O., Calabrese, D., Cartacci, M., Cicchetti,  
557 A., Clifford, S. M., Edenhofer, P., Farrell, W. M., et al. Radar soundings of the  
558 subsurface of Mars. *Science*, 310(5756):1925-1928, 2005.

559 Plaut, J. J., Picardi, G., Safaeinili, A., Ivanov, A. B., Milkovich, S. M., Cicchetti, A.,  
560 Kofman, W., Mouginot, J., Farrell, W. M., Phillips, R. J., et al. Subsurface radar  
561 sounding of the south polar layered deposits of Mars. *Science*, 316(5821):92-95, 2007.

562 Pommerol, A., Kofman, W., Audouard, J., Grima, C., Beck, P., Mouginot, J., Herique,  
563 A., Kumamoto, A., Kobayashi, T., and Ono, T. Detectability of subsurface interfaces in  
564 lunar maria by the LRS/SELENE sounding radar: Influence of mineralogical  
565 composition. *Geophys. Res. Lett.*, 37(3), 2010.

566 Porcello, L. J. et al., "The Apollo lunar sounder radar system," in *Proceedings of the*  
567 *IEEE*, vol. 62, no. 6, pp. 769-783, June 1974, doi: 10.1109/PROC.1974.9517.

568 Rust, A., Russell, J., and Knight, R. Dielectric constant as a predictor of porosity in dry  
569 volcanic rocks. *J. Volcanol. Geoth. Res.*, 91(1):79-96, 1999.

570 Shkuratov, Y. G. and Bondarenko, N. V. Regolith layer thickness mapping of the moon  
571 by radar and optical data. *Icarus*, 149:329-338, 2001.

572 Williams, K. K. and Zuber, M. T. Measurement and analysis of lunar basin depths from  
573 clementine altimetry. *Icarus*, 131(1):107-122, 1998.

#### 574 **Figure legends**

575 Figure 1 An example of received waveforms. This 327.68 $\mu$ s long time-series of a  
576 reflected echo was received at 00:57:15.181 UTC on May 4, 2008 when SELENE  
577 was flying over Mare Imbrium, i.e., (40.226N $^\circ$ , 345.304E $^\circ$ ) in the selenographic  
578 coordinate. It is filtered and resampled as described in the text.

579 Figure 2 (a) A-scope of the reflected echo of Fig. 1. We used the 2<sup>nd</sup> term of Eq. (8)  
580 for  $x$ -axis instead of  $d_A$ . (b) A zoom-in plot of Fig. 2(a). The first three  
581 reflections including the Moon's surface are clearly seen.

582 Figure 3 (a) B-scan over Mare Imbrium at the selenographic longitude of 345.3E $^\circ$ .  
583 The origin of the apparent depth is taken at the Moon's surface assuming the  
584 averaged radius of the Moon to be 1737.4km. (b) Another B-scan image at the  
585 selenographic longitude of 345.0E $^\circ$ . Several strong echoes of parabolic shape are  
586 due to craters nearby. (c) Taking running means highlighted the subsurface  
587 reflectors especially for those starting from the horizontal black arrows, which

588 continue to  $\sim 42^\circ$ .

589 Figure 4 The two-layer model adopted by this study. The surface and subsurface  
590 reflection are  $P_{rs}$  [W] and  $P_{rss}$  [W], respectively.  $R$  [m] and  $R_D$  [m] are  
591 respectively the altitude of the spacecraft and the **true** depth to the subsurface  
592 reflector. Both relative magnetic permeability  $\mu$  and permittivity  $\varepsilon$  between  
593 SELENE and the Moon's surface are assumed to be unity, while those of the 1<sup>st</sup>  
594 layer are unity and  $\varepsilon_1$ . The electrical conductivity of the 1<sup>st</sup> layer is  $\sigma_1$ , and the  
595 bulk permittivity of the 2<sup>nd</sup> layer is  $\varepsilon_2$ .

596 Figure 5 The flow chart of data analysis of this study.  $\rho$ ,  $p$  and  $\delta_l$  denote density,  
597 porosity and loss tangent of the 1st layer, respectively, while  $\rho_{\text{grain}}$  **indicates the**  
598 **density pertaining to the solid material itself**. As for  $\varepsilon_1$ ,  $\sigma_1$  and  $\varepsilon_2$ , refer to the  
599 caption of Fig. 4.

600 Figure 6 The topographic map of the northern hemisphere on the **near** side of the Moon.  
601 The base map was downloaded from Geospatial Information Authority of Japan  
602 ([http://gisstar.gsi.go.jp/selene/Maps/Stereo\\_En-800.tif.zip](http://gisstar.gsi.go.jp/selene/Maps/Stereo_En-800.tif.zip)), which is jointly  
603 operated by National Astronomical Observatory of Japan and Japan Aerospace

604 Exploration Agency. The four red ellipses denote the location of the target areas

605 of this study.

606 Figure 7 The stacked A-scope.  $P_{\text{RSS}}$  indicates the location of the subsurface echo.

607 Figure 8 Radargrams of Mare Serenitatis for (a) 20 – 25°N and (b) 25 – 30°N.

608 Figure 9 Estimates of  $\varepsilon_1$  (red),  $\varepsilon_2$  (blue) and  $\varepsilon_{\text{grain}}$  of Mare Serenitatis for (a) 20 – 25°N

609 and (b) 25 – 30°N. The regional representatives of  $\varepsilon_{\text{grain}} = 6.49$  (for 20 – 25°N)

610 and 6.39 (for 25 – 30°N) are shown by horizontal green lines. The vertical error

611 bars for  $\varepsilon_1$  and  $\varepsilon_2$  show 95% confidence intervals, while horizontal error bars

612 denote their spatial extent.

613 Figure 10 Radargrams of Oceanus Procellarum for (a) 40 – 45°N and (b) 45 – 50°N.

614 Figure 11 Estimates of  $\varepsilon_1$  (red),  $\varepsilon_2$  (blue) and  $\varepsilon_{\text{grain}}$  of Oceanus Procellarum for (a) 40 –

615 45°N and (b) 45 – 50°N. The regional representatives, i.e.,  $\varepsilon_{\text{grain}} = 6.41$  (for 40 –

616 45°N) and 6.29 (for 45 – 50°N) are shown by horizontal green lines. The vertical

617 error bars for  $\varepsilon_1$  and  $\varepsilon_2$  show 95% confidence intervals, while horizontal error bars

618 denote their spatial extent.

619 Figure 12 Radargrams of Mare Imbrium for (a) 35 – 40°N and (b) 40 – 45°N.

620 Averaged B-scan images are plotted.

621 Figure 13 Estimates of  $\varepsilon_1$  (red),  $\varepsilon_2$  (blue) and  $\varepsilon_{\text{grain}}$  of Mare Imbrium for (a) 35 – 40°N  
622 and (b) 40 – 45°N.  $\varepsilon_{\text{grain}} = 6.60$  (for 35 – 40°N) and 6.56 (for 40 – 45°N) are  
623 values representative of this region, while  $\varepsilon_1$ 's are latitudinal averages. The  
624 vertical error bars for  $\varepsilon_1$  and  $\varepsilon_2$  show 95% confidence intervals, while horizontal  
625 error bars denote their spatial extent.

626 Figure 14 Radargrams of Mare Crisium for (a) 10 – 15°N and (b) 15 – 20°N.

627 Figure 15 Estimates of  $\varepsilon_1$  (red),  $\varepsilon_2$  (blue) and  $\varepsilon_{\text{grain}}$  of Mare Crisium for (a) 10 – 15°N  
628 and (b) 15 – 20°N. The regional representatives of  $\varepsilon_{\text{grain}} = 6.17$  (for 10 – 15°N)  
629 and 6.29 (for 15 – 20°N) are shown by horizontal green lines. The vertical error  
630 bars for  $\varepsilon_1$  and  $\varepsilon_2$  show 95% confidence intervals, while horizontal error bars  
631 denote their spatial extent.

632 Figure 16 Correlation between the bulk permittivity of the 1<sup>st</sup> layer,  $\varepsilon_1$ , and the surface

633 metal content in lunar maria under study. A regression line is drawn in red. The  
634 error bars of  $\varepsilon_1$  were calculated using values of  $\varepsilon_1$  and their 95% confidence  
635 intervals shown in Figs. 9, 11, 13, and 15.

636 Figure 17 Correlation between the bulk porosity of the 1<sup>st</sup> layer,  $\rho$ , and the formation

637 age of each lunar mare **under study**.

# Figures

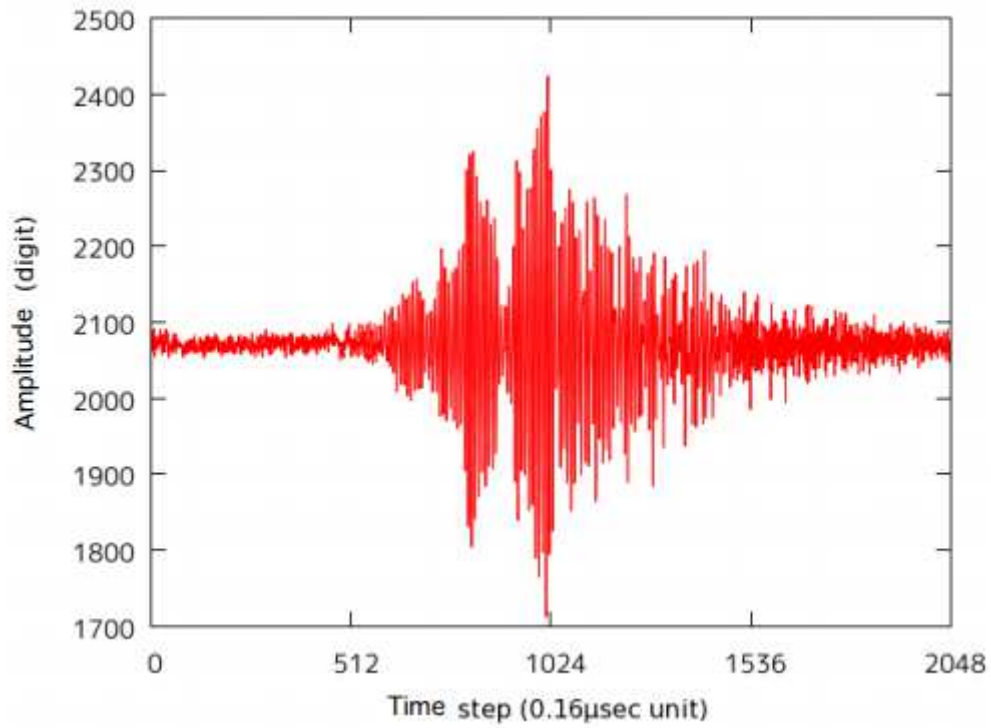


**Figure 1**

An example of received waveforms. This 327.68 s long time-series of a reflected echo was received at 00:57:15.181 UTC on May 4, 2008 when SELENE was flying over Mare Imbrium, i.e., (40.226N°, 345.304E°) in the selenographic coordinate. It is filtered and resampled as described in the text.

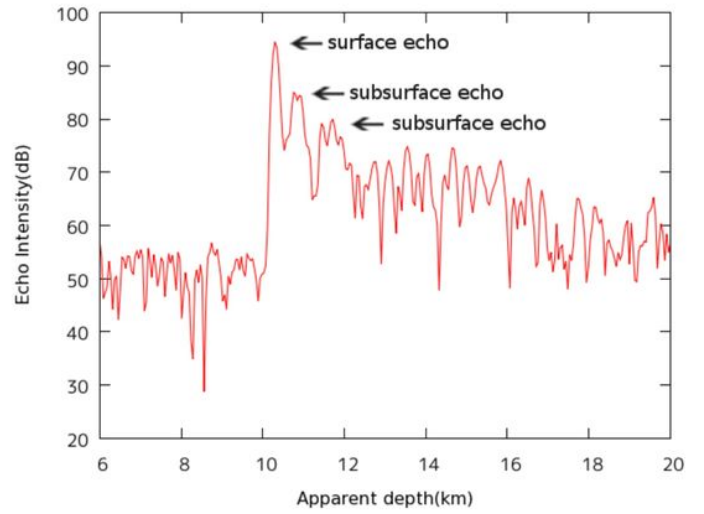
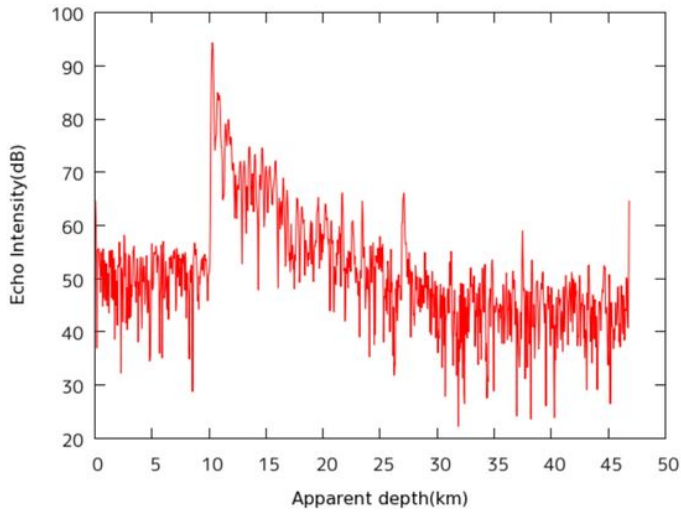


**Figure 2**

(a) A-scope of the reflected echo of Fig. 1. We used the 2nd term of Eq. (8) for x-axis instead of  $dA$ . (b) A zoom-in plot of Fig. 2(a). The first three reflections including the Moon's surface are clearly seen.

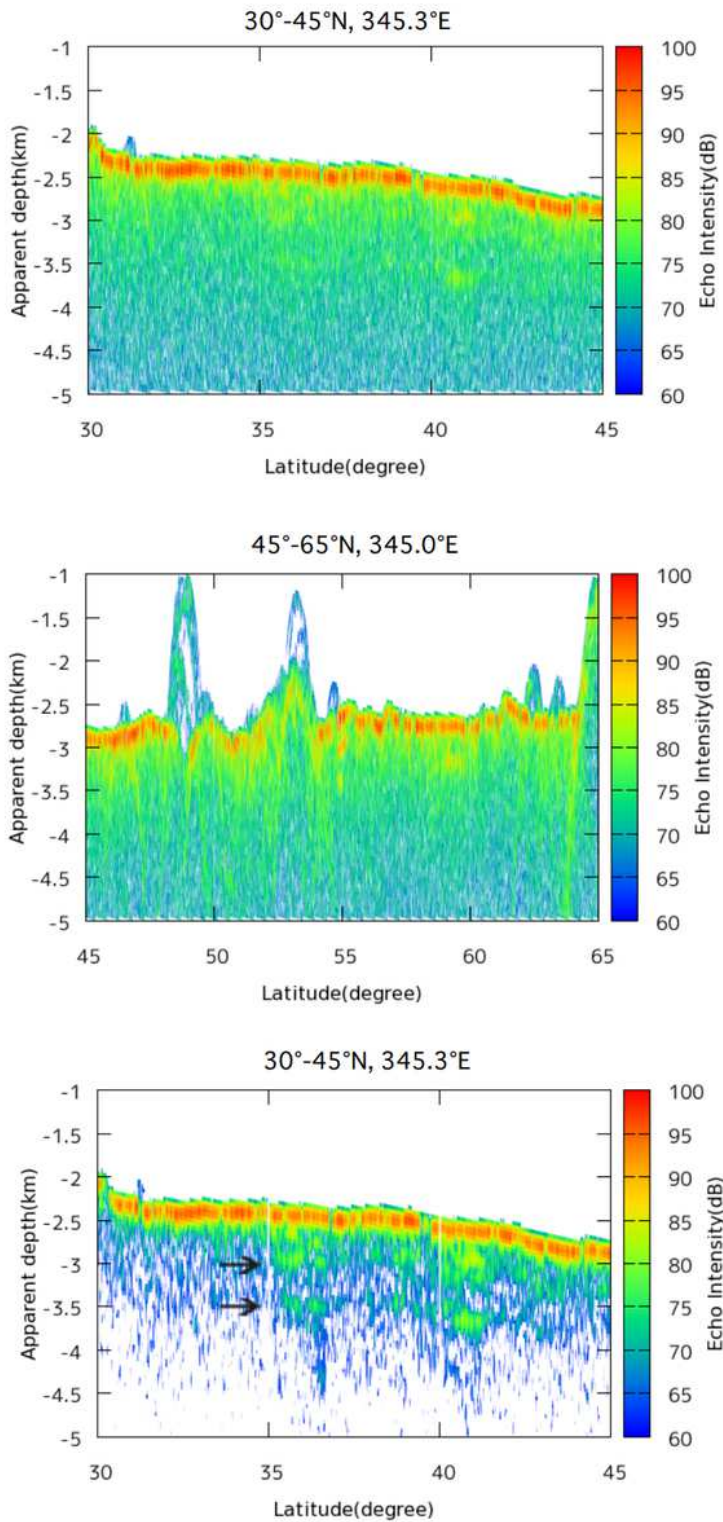


**Figure 3**

(a) B-scan over Mare Imbrium at the selenographic longitude of 345.3°E. The origin of the apparent depth is taken at the Moon's surface assuming the averaged radius of the Moon to be 1737.4 km. (b) Another B-scan image at the selenographic longitude of 345.0°E. Several strong echoes of parabolic shape are due to craters nearby. (c) Taking running means highlighted the subsurface reflectors especially for those starting from the horizontal black arrows, which continue to ~42°N.

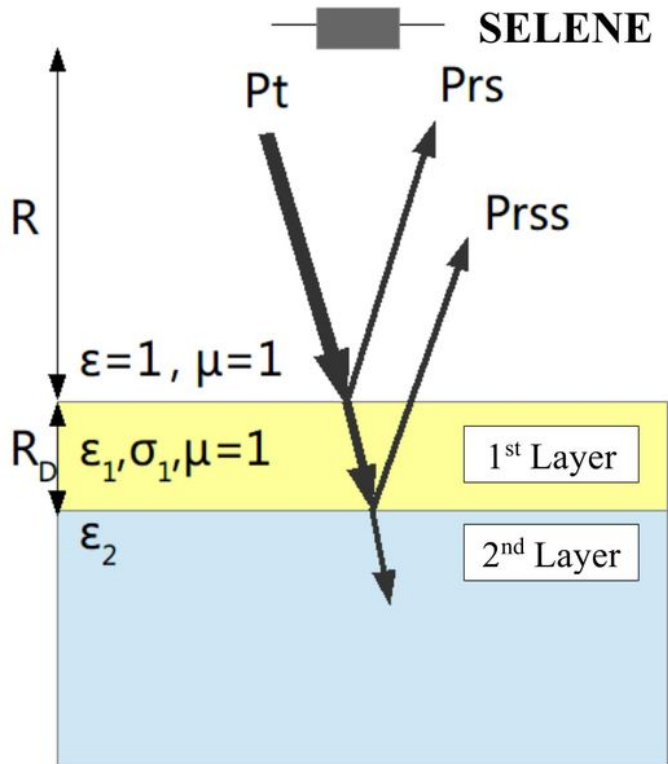


**Figure 4**

The two-layer model adopted by this study. The surface and subsurface reflection are  $P_{rs}$  [W] and  $P_{rss}$  [W], respectively.  $R$  [m] and  $R_D$  [m] are respectively the altitude of the spacecraft and the true depth to the subsurface reflector. Both relative magnetic permeability  $\mu$  and permittivity  $\epsilon$  between SELENE and the Moon's surface are assumed to be unity, while those of the 1st layer are unity and  $\epsilon_1$ . The electrical conductivity of the 1st layer is  $\sigma_1$ , and the bulk permittivity of the 2nd layer is  $\epsilon_2$ .

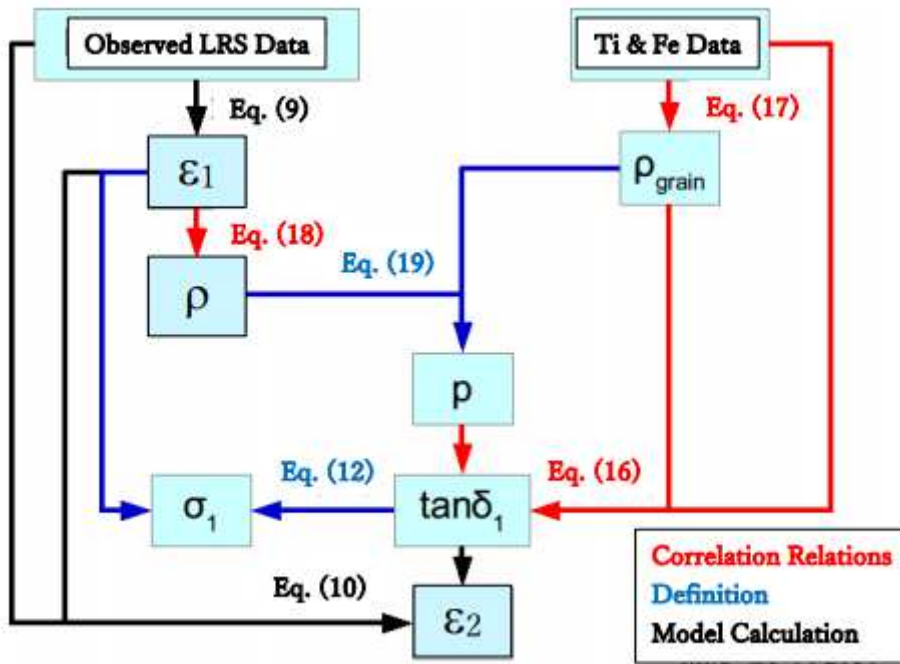


Figure 5

The flow chart of data analysis of this study.  $\epsilon_1$ ,  $p$  and  $\tan\delta_1$  denote density, porosity and loss tangent of the 1st layer, respectively, while  $\rho_{\text{grain}}$  indicates the density pertaining to the solid material itself. As for  $\epsilon_1$ ,  $\sigma_1$  and  $\epsilon_2$ , refer to the caption of Fig. 4.

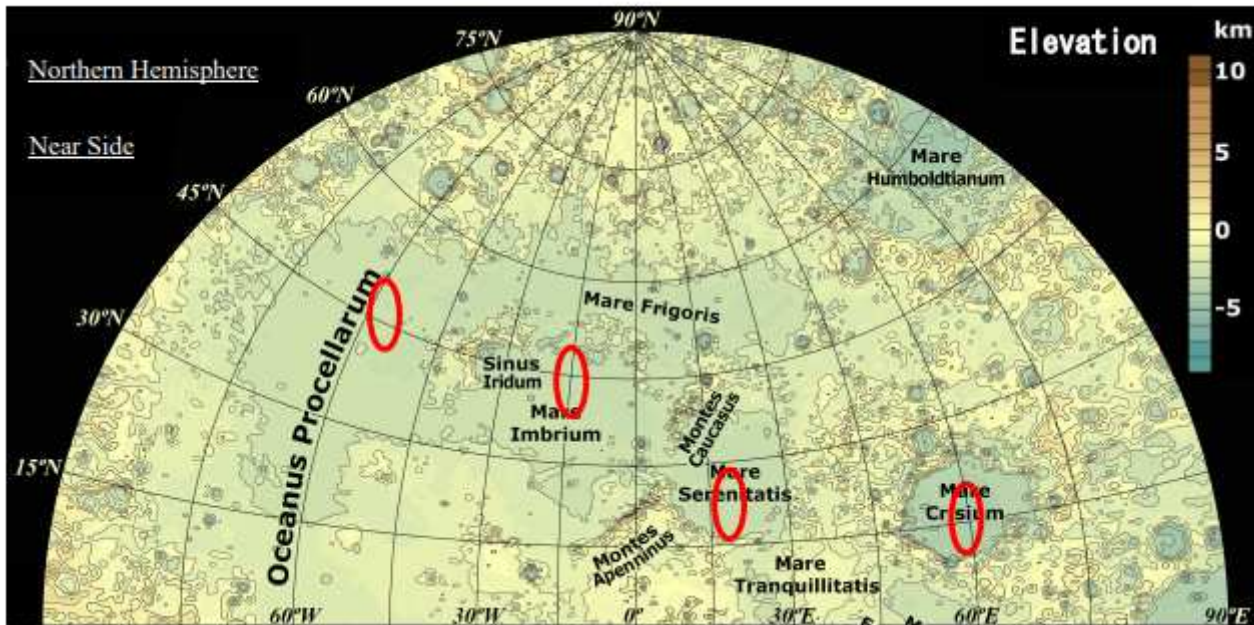


Figure 6

The topographic map of the northern hemisphere on the near side of the Moon. The base map was downloaded from Geospatial Information Authority of Japan

([http://gisstar.gsi.go.jp/selene/Maps/Stereo\\_En-800.tif.zip](http://gisstar.gsi.go.jp/selene/Maps/Stereo_En-800.tif.zip)), which is jointly operated by National Astronomical Observatory of Japan and Japan Aerospace Exploration Agency. The four red ellipses denote the location of the target areas of this study.

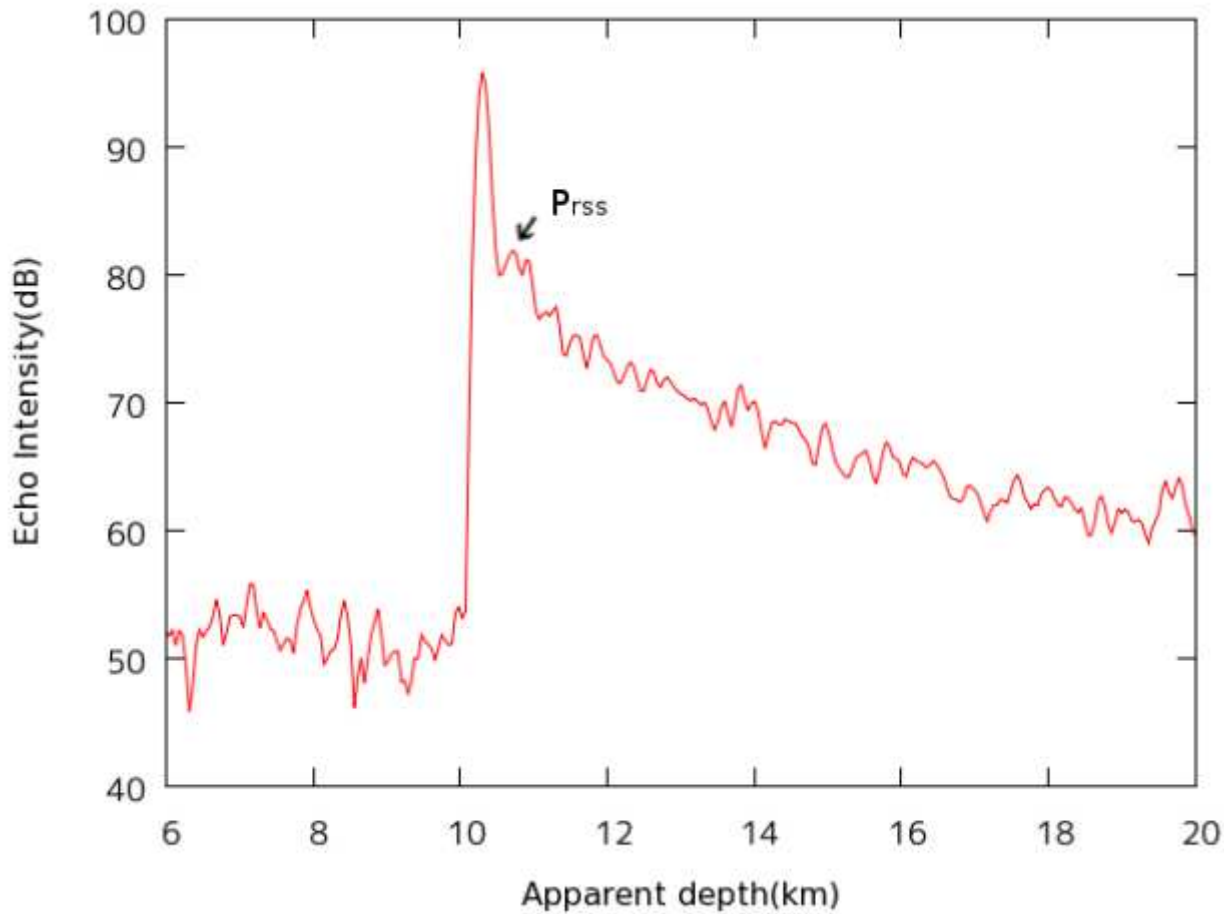


Figure 7

The stacked A-scope.  $P_{r_{ss}}$  indicates the location of the subsurface echo.

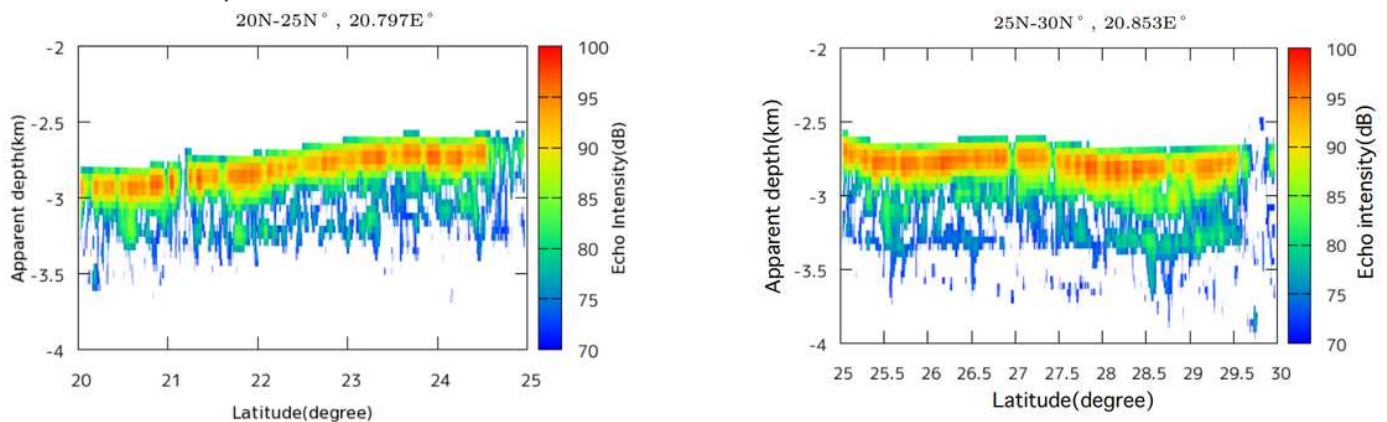
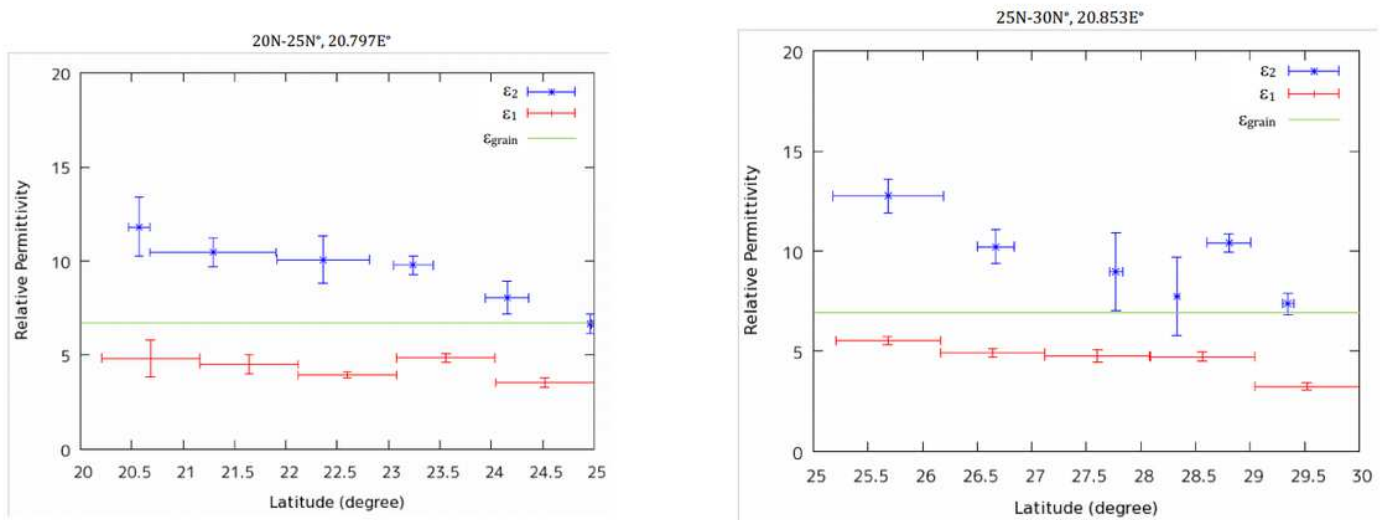


Figure 8

Radargrams of Mare Serenitatis for (a) 20 – 25oN and (b) 25 – 30oN.



**Figure 9**

Estimates of  $\epsilon_1$  (red),  $\epsilon_2$  (blue) and  $\epsilon_{\text{grain}}$  of Mare Serenitatis for (a) 20 – 25oN and (b) 25 – 30oN. The regional representatives of  $\epsilon_{\text{grain}} = 6.49$  (for 20 – 25oN) and  $6.39$  (for 25 – 30oN) are shown by horizontal green lines. The vertical error bars for  $\epsilon_1$  and  $\epsilon_2$  show 95% confidence intervals, while horizontal error bars denote their spatial extent.

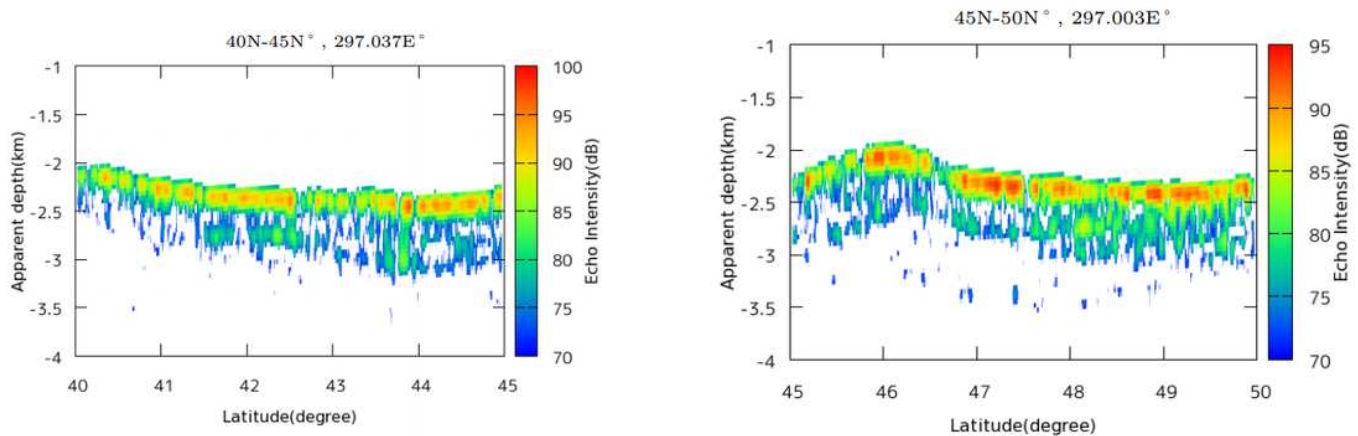


**Figure 10**

Radargrams of Oceanus Procellarum for (a) 40 – 45oN and (b) 45 – 50oN.

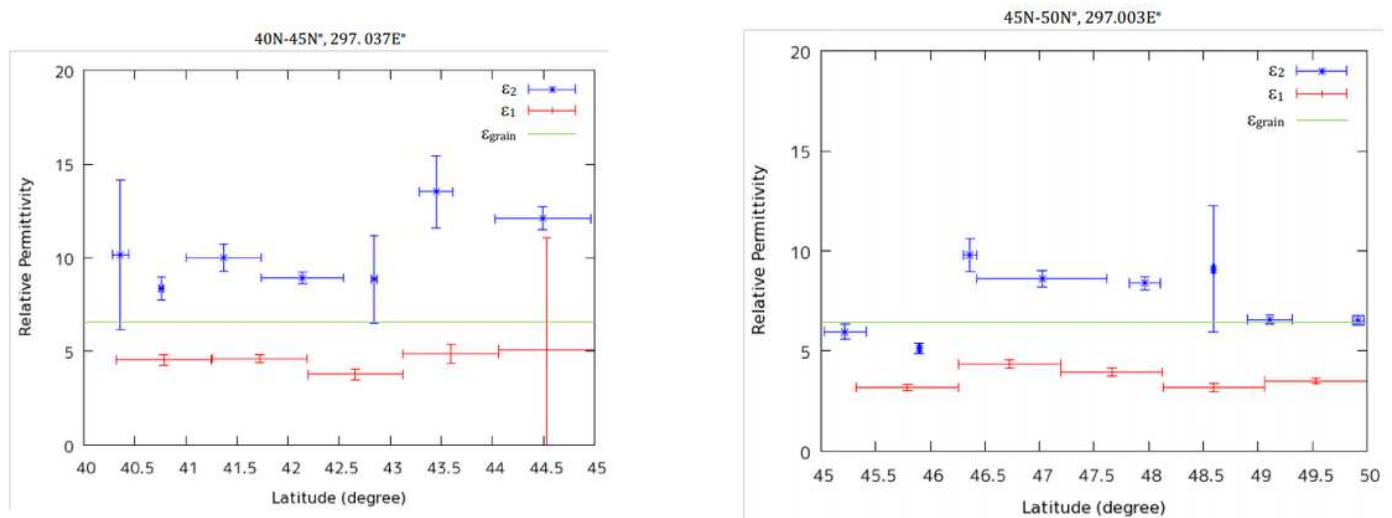


**Figure 11**

Estimates of  $\epsilon_1$  (red),  $\epsilon_2$  (blue) and  $\epsilon_{\text{grain}}$  of Oceanus Procellarum for (a) 40 – 45oN and (b) 45 – 50oN. The regional representatives, i.e.,  $\epsilon_{\text{grain}} = 6.41$  (for 40 – 45oN) and  $6.29$  (for 45 – 50oN) are shown by horizontal green lines. The vertical error bars for  $\epsilon_1$  and  $\epsilon_2$  show 95% confidence intervals, while horizontal error bars denote their spatial extent.

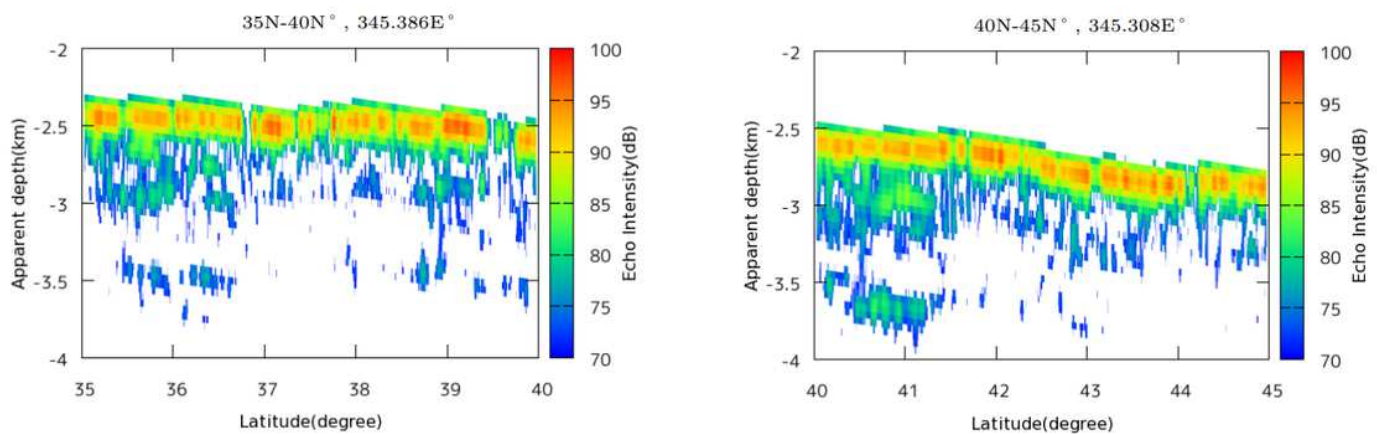


**Figure 12**

Radargrams of Mare Imbrium for (a) 35 – 40oN and (b) 40 – 45oN. Averaged B-scan images are plotted.

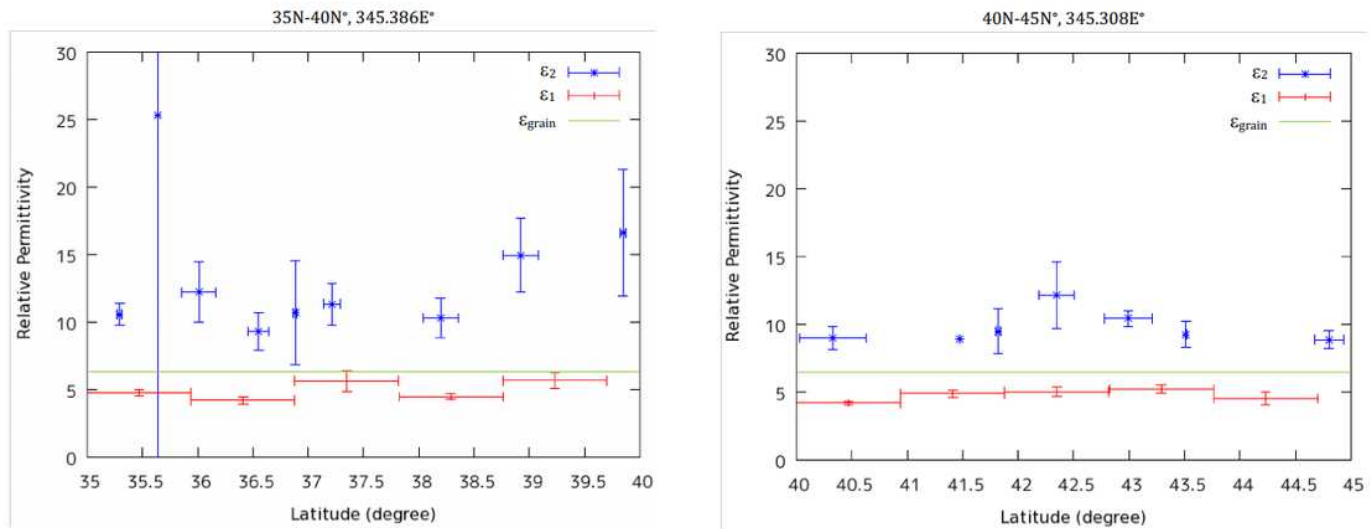


**Figure 13**

Estimates of  $\epsilon_1$  (red),  $\epsilon_2$  (blue) and  $\epsilon_{\text{grain}}$  of Mare Imbrium for (a) 35 – 40oN and (b) 40 – 45oN.  $\epsilon_{\text{grain}} = 6.60$  (for 35 – 40oN) and 6.56 (for 40 – 45oN) are values representative of this region, while  $\epsilon_1$ 's are latitudinal averages. The vertical error bars for  $\epsilon_1$  and  $\epsilon_2$  show 95% confidence intervals, while horizontal error bars denote their spatial extent.

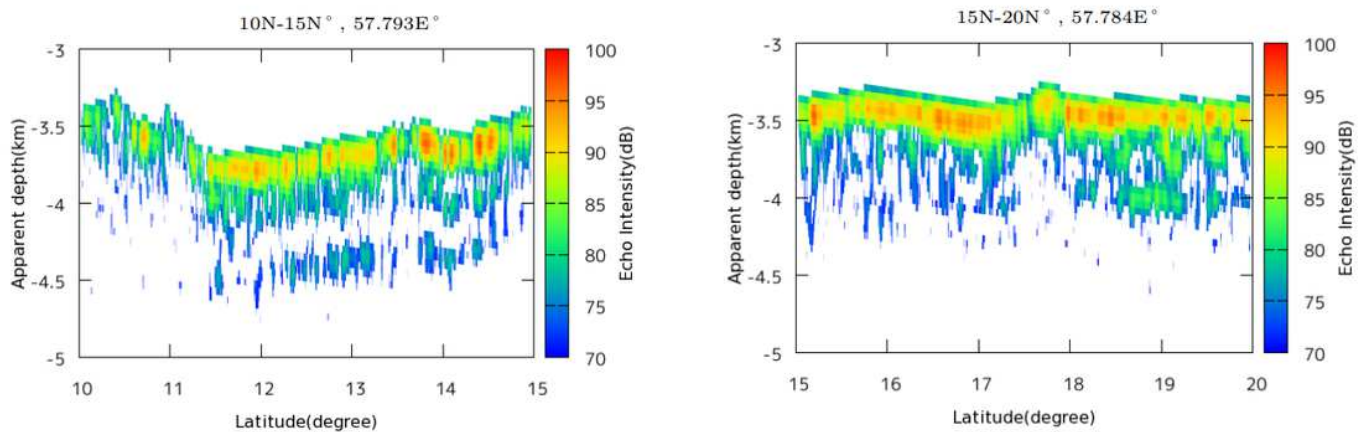


**Figure 14**

Radargrams of Mare Crisium for (a) 10 – 15oN and (b) 15 – 20oN.

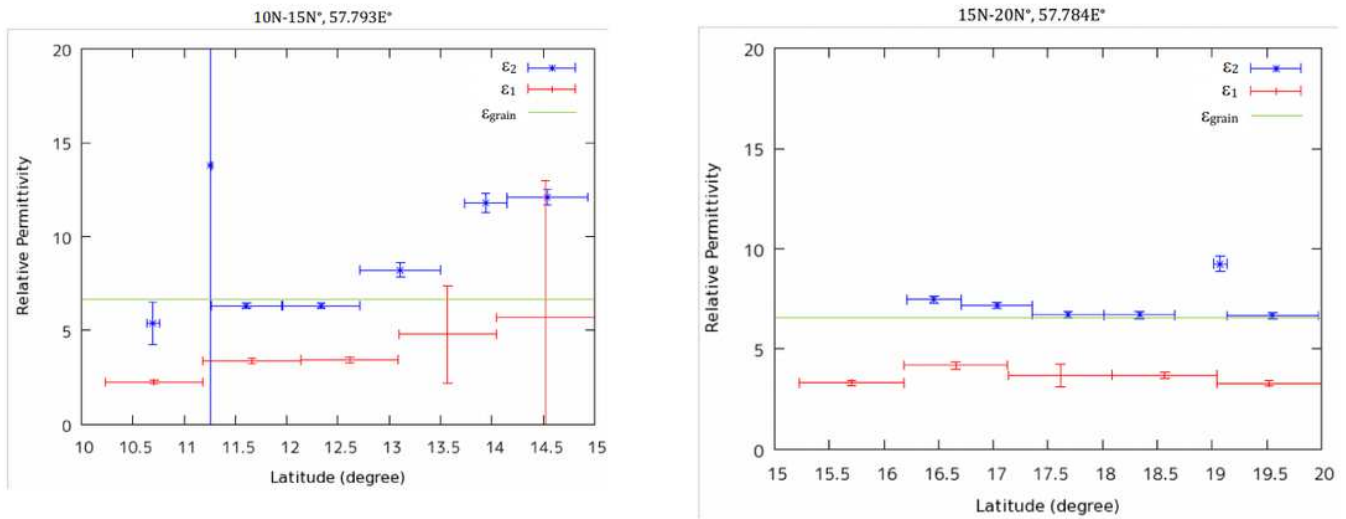


Figure 15

Estimates of  $\epsilon_1$  (red),  $\epsilon_2$  (blue) and  $\epsilon_{\text{grain}}$  of Mare Crisium for (a) 10 – 15oN and (b) 15 – 20oN. The regional representatives of  $\epsilon_{\text{grain}} = 6.17$  (for 10 – 15oN) and  $6.29$  (for 15 – 20oN) are shown by horizontal green lines. The vertical error bars for  $\epsilon_1$  and  $\epsilon_2$  show 95% confidence intervals, while horizontal error bars denote their spatial extent.

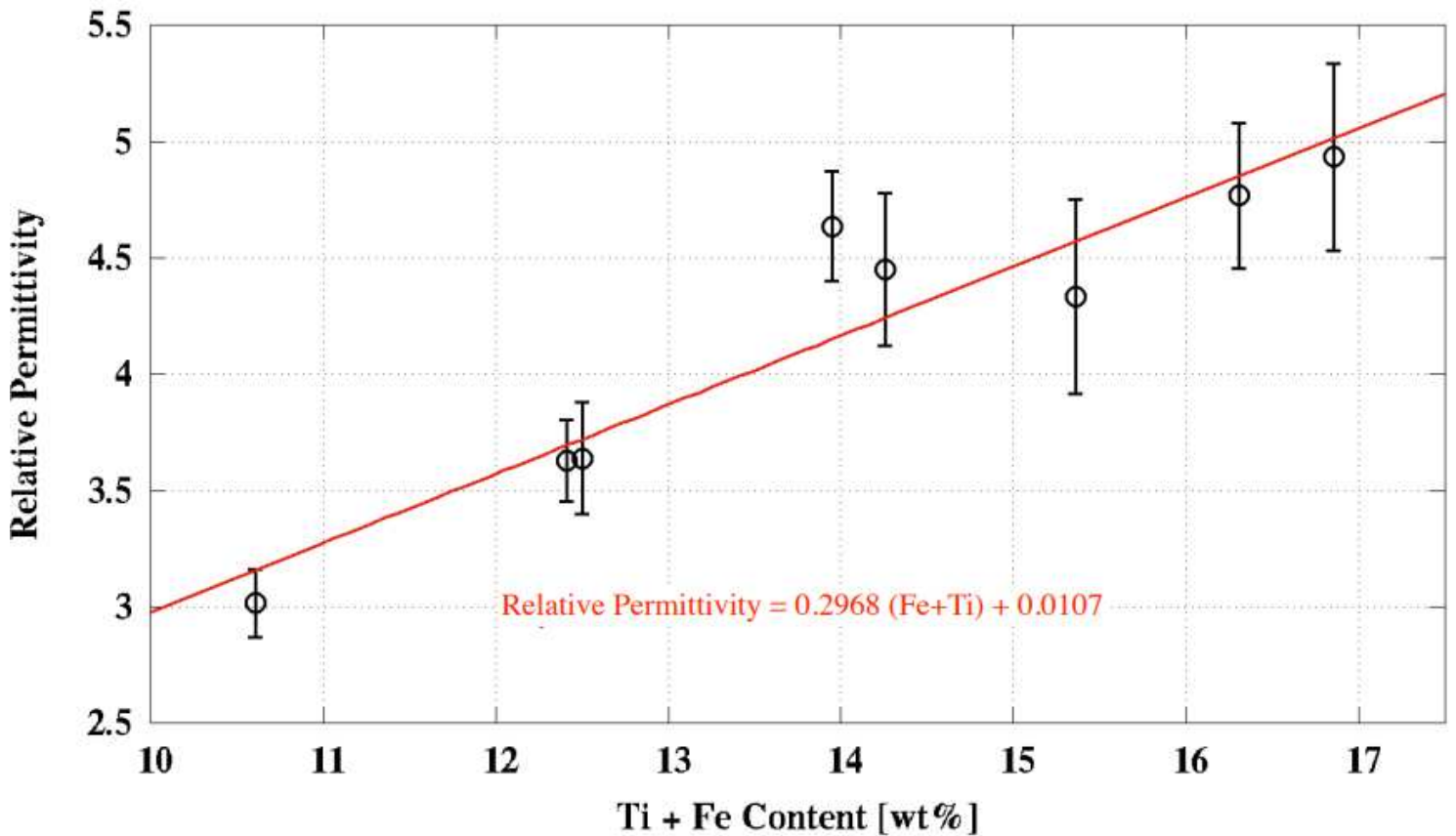


Figure 16

Correlation between the bulk permittivity of the 1st layer,  $\epsilon_1$ , and the surface metal content in lunar maria under study. A regression line is drawn in red. The error bars of  $\epsilon_1$  were calculated using values of  $\epsilon_1$  and their 95% confidence intervals shown in Figs. 9, 11, 13, and 15.

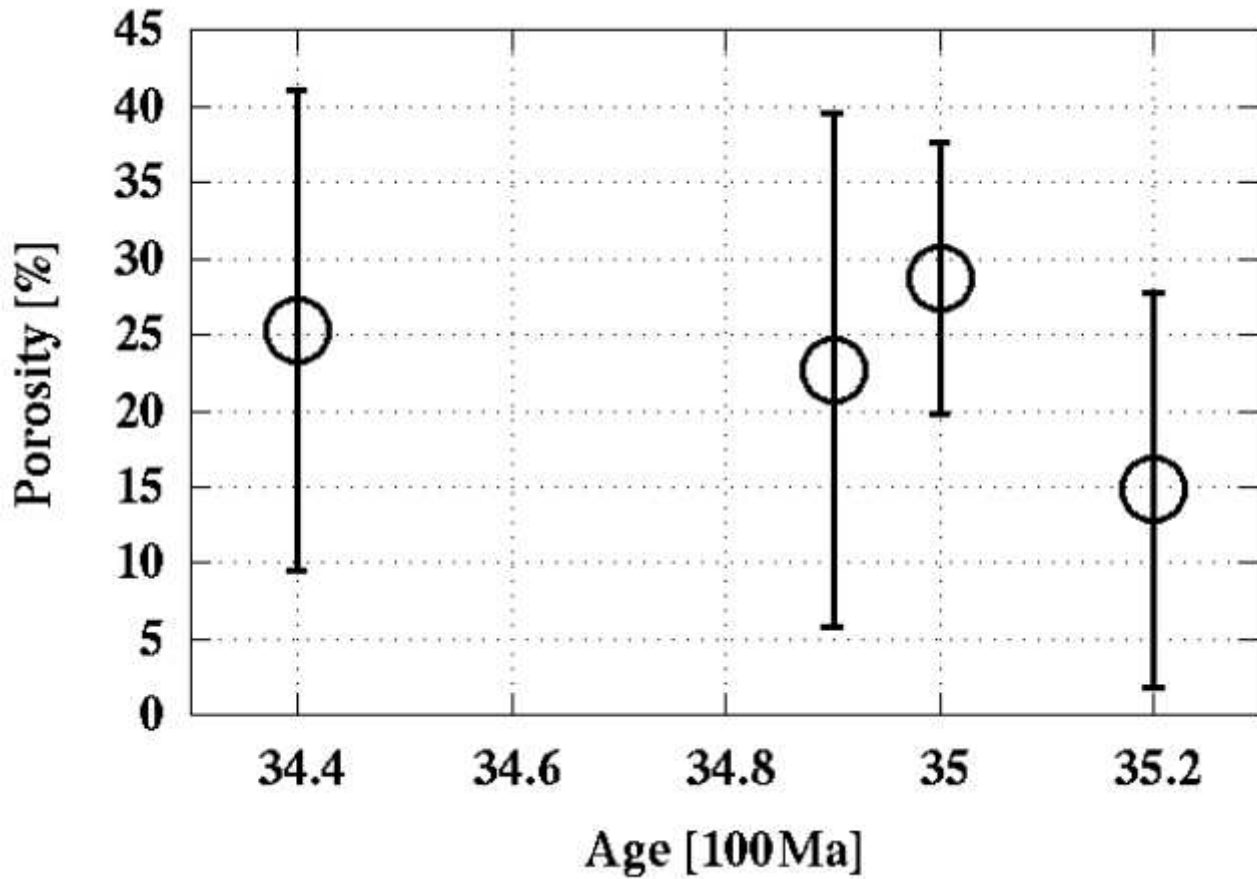


Figure 17

Correlation between the bulk porosity of the 1st layer,  $\epsilon_1$ , and the formation age of each lunar mare under study.

## Supplementary Files

This is a list of supplementary files associated with this preprint. Click to download.

- [Table1R2.pdf](#)
- [GraphicalAbsR2.pdf](#)